Aalborg Universitet

Evaluating the different boundary conditions to simulate airflow and heat transfer in Double-Skin Facade

Ahmadi, Javad; Mahdavinejad, Mohammadjavad; Larsen, Olena Kalyanova; Zhang, Chen; Zarkesh, Afsaneh; Asadi, Somayeh

Evaluation the different boundary conditions to simulate airflow and heat transfer in Double-Skin Facade (DSF)

Javad Ahmadi[1], Mohammadjavad Mahdavinejad[1], Olena Kalyanova Larsen[2], Chen Zhang[2], Afsaneh Zarkesh[1], Somayeh Asadi[3]

1. Highperformance Architecture Laboratory, Department of Architecture, Tarbiat Modares University, Jalal-e Al Ahmad Highway, Nasrbridge, Tehran, Iran
2. Department of Built Environment, Faculty of Engineering and Science, Division of Architectural Engineering, Aalborg University, Aalborg, Denmark
3. Department of Architectural Engineering, Pennsylvania State University, PA 16801, USA

Abstract

The CFD simulation accuracy mostly depends on the appropriate setting of boundary conditions and numerical simulation parameters. This study shows the influence of two types of boundary condition settings on the CFD simulation results of Double-Skin Façade (DSF) for a specific problem. These two boundary settings are the constant temperature on the DSF surfaces called Boundary A, and Boundary B is defined via solar radiation using the Discrete Ordinate radiation Model (DOM). The paper verified both the numerical simulations using the experimental data. Comparing the numerical results of two types of boundaries with experimental data shows that both cases underestimated the values lower than 5.2 K and 0.1 m/s for the temperature and velocity respectively at the regarded measured points. Boundary A gives more accurate temperature prediction results while Boundary B shows velocity magnitude closer to the measurements in the middle height of the cavity; the average temperature and velocity differences between the two boundary types are 0.6 K and, 0.003 m/s respectively which are negligible. Finally, the selection of boundary conditions depends on study purposes, however, when the DSF is equipped with blinds and if there is not enough data in hand but the exact value of solar irradiation, using the Boundary B approach is suggested; it can provide reasonable results associated with multi-type of thermal boundary conditions at the same time. Furthermore, if the goal is to investigate the flow pattern in the DSF, Boundary B is argued to perform better than the constant temperature boundary condition.

Keywords:

Double-Skin Façade, boundary conditions, thermal performance, airflow, Irradiation

1   Introduction

The building energy demand is closely linked to a building envelope's thermal performance. Several measures can be taken to enhance these envelopes. One of them is adding internal ventilated air layers such as Double-Skin Facades (DSFs) (Agathokleous and Kalogirou 2016; Barbosa and Ip 2014). DSFs have become more popular because they allow for more architectural design freedom and the use of wind-protected external shading systems in high-rise buildings (Poizaris 2004). The appropriate behaviour of DSF requires numerous design considerations related to the dimensions and thermophysical properties of the façade elements. The design of a DSF with a naturally ventilated cavity, where the thermal process and the flow mechanism influence each other, is considered one of the field's challenges.

Multiple studies were carried out to evaluate the performance of ventilated facades. Several publications address their question experimentally (Anđelković et al. 2015; Gaillard et al. 2014; Zöllner et al. 2002). Nowadays, given the vast capabilities provided by advanced Computational Fluid Dynamics (CFD) tools, the number of studies done using this method has grown enormously (Ibañez-Puy et al. 2017). CFD can predict the airflow and heat transfer of DSFs. Thus, a CFD analysis could be one of the most important tools to predict the behaviour of DSF and help architects make decisions during the design process (Pasut and Carli 2012). CFD is one of the best alternative methods for costly and time-consuming laboratory studies (Chen and Srebric 2002; Pasut and Carli 2012). According to Chen and Srebric (2002), modelling and the accuracy of CFD simulations strongly depend on the appropriate setting of boundary conditions and numerical simulation parameters. In this regard, the important thing is that there is no standard procedure or benchmark case for CFD simulation of DSF. Thus, it is essential to consider an appropriate thermal boundary condition setting that enables correct temperature distribution calculations in an indoor environment (Yuan and Srebric 2004). It is challenging that many studies do not provide explicit information about their simulation method and the boundary conditions.

Many CFD studies are focusing on the performance of the air layer envelopes (Zhang and Yang 2019a). If it is essential to concentrate on airflow and mass

flow simulation, thus it is enough to have surface temperatures known (Iyi et al. 2014; Ospir et al. 2012; Hiroyuki et al. 1974; Zeng et al. 2012). Some studies were focused on the modelling of airflow patterns inside the cavities regardless of their opacity. In these cases, the authors use heat flux boundary conditions added to the domain directly to solve a buoyant flow inside the cavity (Desrayaud et al. 2013; Jiru et al. 2011; Kimouche et al. 2017; Kiwan and Khodier 2008; Manz 2003). Some studies have used temperature thermal boundary conditions for the studying of DSF performance (Pomponi et al. 2016). Iyi et al. (2014) have used constant temperature boundary conditions on both glass and blind surfaces to evaluate the most efficient CFD modelling technique of DSFs (Iyi et al. 2014). Pasut and Carli (Pasut and Carli 2012) used the same method to compare the performance of most used turbulent models $k-\varepsilon$ and $k-\omega$ in terms of accuracy. Coussirat et al. (Coussirat et al. 2008) also analyzed different models of turbulence and radiation models to simulate the thermal behaviours of a double-glazed façade using CFD. They also used constant temperature thermal boundary conditions to establish their analysis. On the other hand, some studies tried to consider the heat source as a volumetric term. Jiru et al. (2011) modelled DSF performance integrating with thermal mass to enhance its thermal performance. They have used volumetric heat flux (W/m^3) to simulate the blinds' heating effect inside the cavity (Jiru et al. 2011).

Using the heat flux dominates the existing research body as the primary boundary condition (Kimouche et al. 2017; Zhang and Yang 2019b); meanwhile, choosing the best boundary condition (both the thermal and radiation types) for open cavities still is a delicate issue (Desrayaud et al. 2013). Furthermore, there is a lack of information on the detailed flow and heat transfer process in DSFs, especially when the blinds are equipped inside the cavity (Zhang and Yang 2019a). Thus it is necessary to utilize suitable tools and methods of defining boundary conditions to clarify and overcome the issues mentioned above.

Besides, including the heat source such as sun radiation has also been the interest of some researchers. Safer et al. (Safer et al. 2005b) simulated the flow and heat transfer inside a naturally ventilated DSF by modelling direct radiation in Fluent. Several authors investigated to understand DSF performance in conjunction with blinds, where the incident solar radiation and the blind angle are the main research problem (Gan 2006; Pasut and Carli 2012; Safer et al.2006). Kim (Kim, 2020) assessed the thermal performance of the different DSF configurations such as cavity

geometry and the use of shading devices in the presence of direct radiation using the STAR CCM+CFD tool. The author's contribution was directly related to the method of defining irradiation values and the direction of incidence angle. Based on modelling direct radiation using CFD tools such as CFX commercial software is one method that is considered applicable for situations where there is not enough measured data, but radiative source intensity and direction are known (Ji et al. 2007). Moghimi et al. (2015) have utilized the ANSYS-Fluent tool using the Discrete Ordinate Model (DOM) and a finite volume method to solve heat transfer and fluid flow inside a solar collector and could enhance the regarded CFD tool's applicability. The authors introduced ray-tracing to solve optical, thermal, and flow features using an integrated approach with detail (Moghimi et al. 2015). Nevertheless, the authors have referred to the difficulties and limitations of their proposed method (Craig et al. 2016; Moghimi et al. 2016, Hazem et al. 2015) evaluated DSF performance using CFD and especially considering DOM. They examined the effect of solar radiation, incidence angle, and slat angle on the thermal properties, as well as, the solar transmission into the interior environment for a DSF equipped with a Venetian blind using ANSYS-Fluent. To do so, it is necessary to model direct radiation in the computational domain. Based on their results, just using DOM makes it possible to consider the effect of multiple parameters at the same time.

According to each study's purpose showing the performance of DSFs (Agathokleous and Kalogirou 2016; Darkwa et al. 2014; Fallahi et al. 2010; Safer et al. 2005a), there could be considered different thermal boundary conditions in CFD simulations. No study has been done so far that provide comprehensive DSF modelling setups in terms of defining different boundary conditions.

Thus, this study aims to provide information for developing and selecting an appropriate DSF system simulation using CFD. Also, the effect of using two types of boundary conditions is another purpose of the study. This paper presents a naturally ventilated DSF simulated by defining two types of thermal boundary conditions; no study used this approach on DSFs yet; then the paper is to demonstrate and discuss the pros and cons of each boundary condition type. To this end, the authors also aim to contribute to the classification of DSF modelling approaches.

2 Materials and method

The case that is being solved for two boundary conditions in this study is extracted from the literature (Mei et al. 2007) with all corresponding dimensions, boundary conditions, and measured data. Then the accuracy of the CFD simulation results is verified using the published experimental data.

2.1 Model description

The façade design was chosen from the study of Mei et al. (2007). In their study, the model includes the following: the outer layer with a 0.012 m thick clear glass pane with dimensions of 1.44 m wide and 2.06 m high comprising an aluminium frame and the glass area is 1.28 m wide 1.91 m high. The air intake and exhaust of the DSF are designed as a commercial grille arrangement to permit airflow through the façade cavity. The grilles are rectangular with 0.24 m high and 1.45 m wide. Each grille has a 0.45 m high space for entering and extracting air from the cavity at a 30-degree angle. The façade inner skin is fitted with double glazing housed within an aluminium frame. The glazing cross-section comprises two panes of Low-E toughened clear glass each 0.006 m thick, separated by an air cavity of width 0.16 m. The dimensions of the inner skin are 1.38 m in 2 m and the glass area is 1.22 m in 1.85 m. The cavity is equipped with Venetian blinds for solar protection.

The blind is made of aluminium and is 2.1 m high and 1.45 m wide. The cavity width is 0.55 m, and the blinds were located at the optimized position of summer condition (Gracia et al. 2015; Gratia and Herde 2004). It means that blinds are positioned at one-third of the outer layer. Figure 1 shows the perspective and cross-sectional scheme of the modelled geometry. All the glass thermal properties and dimensions are shown in the following section.

The ambient air temperature and outside temperature were constant and equal to 293.15 K during the experiments. The study used ten thermometers (two of them were located on the inner side of glasses) to measure the temperature at the cavity's middle height. Seven anemometers were positioned at a 0.01 m downside of the equipped thermometers at the same positions. The positions of the sensors, inner, outer layers, and the blinds are shown in Figure 2.

2.2 Numerical modelling

The study used a 2D steady-state simulation utilizing ANSYS Fluent v.18 CFD package. The airflow pattern is almost bidirectional in the problems with natural ventilation and with symmetrical vertical configurations in the core region of the DSF. This behaviour was proven experimentally (Betts and Bokhari 2000) and utilized by some authors (Safer et al. 2006). According to Pasut and Carli (Pasut and Carli 2012), a 2D model results are almost like a 3D model even with remarkable computational time-saving. Another study was done by Iyi et al. (Iyi et al. 2014) in terms of the modelling technique of DSF using CFD. They showed four configurations of the DSF geometry modelling strategies associated with and without outdoor and indoor environments. For all four modelling strategies employed in their study, there appears to be no essential difference in the key parameters responsible for the DSF performance, provided all indoor and outdoor boundary conditions are defined accurately. However, considering external and internal environments can be useful if the problem mainly is to investigate the behaviour of these environments. But, it will be more cost-effective and also save computational effort by not including these domains in computations if the primary need is just to numerically model the DSF channel (Iyi et al. 2014). The "isolation" approach (i.e. only modelling of the cavity domain) was also used in the previous researchers' study as well (Gavan et al. 2007; Guardo et al. 2009; Guardo et al. 2011; Kimouche et al. 2017; Kuznik et al. 2011; Safer et al. 2005b; Zhang and Yang 2019b). The simulations used the second-order upwind scheme for all of the variables except pressure. The SIMPLE algorithm for coupling the pressure and momentum equations, the Body-Force Weighted scheme for the pressure discretization were selected (ANSYS Inc 2016). The sum of absolute normalized residuals for all of the cells in the domain considered less than 10^{-6} for energy and 10^{-4} for other variables, the solution was considered converged (Zhang and Chen 2007). In the problem, the Reynolds number is generally at the range of 10^4. The Rayleigh numbers of the cases investigated in this paper are in the range of high order of 10^9 to 10^{10} (Iyi et al. 2014; Ji et al.2007); thus $k-\varepsilon RNG$ turbulence model was selected to solve turbulent flow in the domain. Based on Pasut and Carli (2012), the chosen turbulence model gives a better prediction than the rest of the models. For solving the Radiative Transport Equation (RTE), the Discrete Ordinate Method (DOM) radiation model was chosen which will be explained more in the following section. The grid dimensions influence the accuracy of CFD results and the value of Y^+. For this study, the Y^+ is considered equal to 1 to create the nearest cell to the blinds and glasses. The Boussinesq approximation was used to calculate air density. All the considered assumptions, which are typical for all the simulations, are shown in Table 1. Table 2 shows the air properties which are used in the simulations. Regarded assumptions and calculations such as Y^+ and first layer distances from solid surfaces are also presented in Table 1-2.

2.3 Boundary conditions

The conducted tests have been modelled numerically with two types of boundary conditions; both are valid physically as the following:

1. The temperature of domain boundary consequent of the acted radiation during the tests mapped on the regarded surfaces as thermal boundaries (glazing and blind surface temperature) known as **Boundary A**
2. The employed radiation introduced directly in the computational domain as known as **Boundary B**

There were three main reasons for choosing the boundary A and B in this study. The temperature boundary condition's setup is simple in terms of application and only requires knowing and defining temperature values. In contrast, radiation boundary conditions are much more complex and require more effort. The second reason is the availability of input information; only the surface temperatures and solar radiation were the two measured parameters, which were available and derived from the literature (Mei et al. 2007). The third reason is related to the modelling of DSF with blinds which makes DSF performance sensitive to direct radiation as the dominant heat source in conjunction with blinds, while the temperature of the blind slats is not easy to measure.

2.3.1 Boundary A descriptions

As mentioned above, in this case, the solar radiation was not directly simulated, but the surface temperatures measured were used as the boundary conditions (Zhai et al. 2008). The initial temperature of the facade was the same as the outside, 293.15 K (Mei et al. 2007). Air ingress and egress are considered as pressure inlet and outlet boundaries, and internal pressure was deemed to be equal to atmospheric pressure, which is zero. The most critical parameter for using this type of boundary condition is accessing valid experimental data for each considered surface. The temperatures on the boundaries were extracted from Mei et al. (Mei et al. 2007) measured data. These values allocated for the surfaces were respectively: the inner surface of the outer glass= 315.88 K, the inner surface of the inner glass= 309.35 K, and for the blinds 310.27 K.

2.3.2 Boundary B descriptions

For the same case (Box-window DSF with 45 degrees blind near the outer layer), all simulation parameters remained unchanged, except the thermal boundary condition types. The external glazing of DSF is exposed to fixed incident radiation of 715 W/m² (Iyi et al. 2014a; Mei et al. 2007b; Pasut and Carli 2012a). The outdoor and indoor air temperatures are set at 293.15 K. As the

inner and outer glasses are in contact with external air, 7.7 W/m²K and 25 W/m²K were considered to convey the heat transfer coefficient following BBRI 2002 (Belgian Building Research Institute 2020).

2.3.3 Radiation modelling

For a better understanding of the impact of the radiation on the DSFs behaviour, the global solar radiation composed by the direct solar radiation (collimated beam) as well as the long-wave radiation of each component (emissions of each DSF surface) of the DSF (internal and external glazing, and blinds) must be modelled accurately (Safer et al. 2004). Cussirat et al. (Coussirat et al. 2008) and Wu et al. (Wu and Lei 2015) focused on the analysis of different radiation models in the evaluation of DSF and heated channel performance using ANSYS-Fluent. As reported in the literature (Wu and Lei 2015), DOM transforms the Radiative Transfer Equation (RTE) into a transport equation for radiation intensity in the spatial coordinates. Furthermore, the DOM radiation model deals with radiative heat transfer and the problems which are involving both grey and non-grey surfaces. Also using DOM enabled the modelling to deduce the transmitted solar flux into the interior environment. This method makes it possible to show the effect of the incident angle of the irradiation inside the cavity (Hazem et al. 2015). So, solar radiation is directly modelled and used as radiation boundary conditions on glazing as a heat source. The radiation modelling consists of solving the Radiative Transfer Equation (RTE), taking into account the direct solar irradiation and long-wave radiation of each component of DSFs along with convection and conduction fields. It is possible to supply the incoming irradiation flux in terms of its magnitude, beam direction, and solid angle over its surface radiative flux. Note that the refractive index of the external medium is assumed to be 1 (ANSYS Inc 2016). Thus, direct radiation is modelled using DOM, but there happen some issues during the solution. The main errors named "ray effect" and "false scattering" errors which is attributed to mesh typology and associated with DOM resolution setting. Overall these issues could be diminished and some considerations reduce their adverse impact on the results, especially if exact simulations are the main study scope (Moghimi et al. 2015; Craig et al. 2016; Moghimi et al. 2016). For the DOM setting to this case $3 \times 200\_6 \times 6$ were selected for Theta, Phi divisions, and, pixelation namely. There was only the solar irradiation value reported by Mei. et.al.(2007) and there was no mention about the fraction between the direct and diffuse amount. Also due to operating the experiment in a controlled space of a room using a solar simulator, the effect of diffuse

4

irradiation would likely be insignificant; referring to Iyi et al. (2014), only direct solar radiation is considered in the CFD model as the diffuse effects were expected to be negligible; thus, only the direct radiation (715 W/m^2) was considered during the simulations. The study used fixed radiance and temperature values to verify the experimental condition of Mei et al. (Iyi et al. 2014; Ji et al. 2007; Mei et al. 2007). The components' radiative characteristics are fundamental, especially for the detailed calculations of solar gains. All the material properties are shown in Table 3. Figure 3 shows an overall scheme of the inputted boundary conditions for Boundary B.

2.4 Meshing properties

A hybrid system of meshing was created for numerical modelling. For both cases, the mesh independence test was carried out. The velocity and temperature of the cavity for the different number of meshes are presented in Figure 4 (a and b). Figure 5 shows the used mesh properties for the simulations. It was tried to apply dense grids around blinds and glazing surfaces as they were critical positions. The latter effort would help to catch the flow and thermal boundary layers correctly.

For both mesh independence tests, the results were approximately the same in terms of meshes' fineness. Table 4 shows all mesh properties. The differences between the average velocities in the cavity were less than 2% for the fine to finest mesh. On the other hand, this difference in the cases of medium to fine was higher than 11%. Similarly, the mesh size has a significant effect on the calculation of the temperature inside the cavity from medium to fine mesh too (around 8 K); from the fine to finest mesh, the difference of the temperatures was around 0.2 K. Thus, to get more precise results a hybrid mesh method with an order of 100000 cells (fine mesh) was selected for the next simulations. The highlighted section presents in Table 4 means the fine meshing chosen to use.

3 Results

3.1 Models verification

First of all, to models verification, the predicted results obtained using Boundary A and B setups were compared with the experimental data. All data were collected in the core of the DSF with sensors arranged from the inner to outer layers (all are shown in Figure 2) and the CFD data were plotted in the same positions.

Figure 6 shows the calculated temperature comparing with each other and with the experimental data associated with the inner, outer

glass and blinds positions. Table 5 shows the differences between calculated temperatures and measured data and the mean bias error of the models have been presented. The surface temperature is a very critical parameter in the modelling of natural convection inside a domain. The surface temperature of DSFs facing the cavity is vital for the development of the boundary layer and the flow regime in the cavity. According to the literature (Giancola et al. 2018; Kalyanova and Heiselberg 2008; Kalyanova Larsen 2008), this parameter must be taken into very precisely since the higher surface temperature the better strength has the buoyancy force and this would affect the entire thermal and flow regimes inside the cavity. This implies the point that any variation of such variable would affect the problem. According to Figure 6, the surface temperature of the inner layer calculated by Boundary B is almost 3.2 K lower than the measurements and this value for the outer layer surface temperature is around 2.9 K lower. These differences would consequence other differences in the air temperature, velocity and flow rate calculations.

According to this figure for both cases, it can be seen that all the predicted temperatures are underestimated (the Mean Bias Error (MBA) for Boundary A -4.9 K and Boundary B -5.2 K) and the absolute percentage error for Boundary A is 1.6% and for Boundary B that is around 1.7%. For all the sensors, Boundary A had less difference than Boundary B comparing to experimental values but the trends of temperature distributions are the same for both the calculations and the measurements. The lowest difference between the calculated air temperature values with measurement data is around 4.2 K which belongs to Boundary A calculations. The maximum difference between the two calculations is 1.3 K, which is related to the first sensor next to the outer layer. The average air temperatures difference between both the boundary types of all sensors is around 0.6 K that is very low. For the Boundary B case, the maximum value that has been calculated is 310.47 K is related to the blind, which has significantly less difference with the measurements (310.27K). There are no significant temperature differences between the two applied boundaries in calculating temperature inside the fluid zone locally, but there are substantial differences between measured and calculated values for both. According to Table 5, it is seen that Boundary A had a better prediction for air temperature than Boundary B in the middle height of the cavity (due to lower absolute differences between calculated Boundary A and the measured data). It must be stated that this range of discrepancies between the results and measurements were also reported in the previous studies (Pasut and Carli 2012; Iyi et al.2014; Ji et

al.2007). The main reasons of which will be discussed in the "Discussions" part.

Figure 7 shows the calculated velocity comparing with each other and with the experimental data. Table 6 shows the absolute differences between the calculations and the measurements. For both cases, the velocity values have increased in the near-wall regions but the values near the inner layer had low rates. Also, the calculated values were close to the measured ones in the inner cavity region. Comparing the numerical results of two types of boundaries with observed velocity data shows that in both cases underestimation is lower than 0.1 m/s. The difference between calculated average air velocities is around 0.003 m/s for both simulations is negligible. Although the values between the results are very negligible as shown in Table 6, from 7 sensors (#1-5) only 2 sensors (#6-7) of Boundary B calculations have shown larger differences than Boundary A comparing with the measurements. The difference in the velocity fields seems to be very small, but generally, the variations of the velocity in naturally ventilated problems are very low and these low values might have significant consequences in other calculated parameters such as flow rates or temperature drop (Kim, 2020).

The values for Boundary A are closer to the real values at the inner part of the blinds; however, at the centre to the outer side of the blinds, that is Boundary B which shows better predictions; the lowest difference between calculations and the measurement is around 0.006 m/s. Overall, it is shown that both the calculations have been able to catch the trend of velocity variations in the middle height of the cavity.

3.2 Convergence
All the numerical parameters and mesh features were considered the same for both boundaries A and B. The computational efforts were tracked precisely to see how much time is needed for each simulation.

Boundary A includes energy, momentum and continuity equations solved by the solver, however, in Boundary B, an extra equation of RTE added to the solutions simultaneously, and that is expected to take a longer time to converge compared to Boundary A. Besides, for Boundary B, increasing the resolutions of incoming direct radiation increases solution time significantly. In this case (Boundary B), the temperature was an unknown variable that the CFD tool had to solve during the calculation. Therefore, in terms of the complexity of solving equations and defining boundary settings, Boundary B needs more effort than Boundary A. The time allocated for Boundary B

calculation is almost 75% higher than Boundary A. Also, the iterations which were considered for Boundary B were nearly 3.7 times higher than Boundary A. This is a noticeable difference that should be noted as the main cost of the simulations.

3.3 Temperature Distributions
The calculated isothermal contours for both Boundary A and B are shown in Figure 8 (a and b). It is shown that the blinds have separated the cavity into two different temperature fields. The temperature distributions in the cavity are almost similar except at the upper parts.

With a specific look, for Boundary A, the heating effect of the constant temperature on the induced airflow mainly occurs in the adjacent outer layers and the blinds. Regardless of the inlet section, there are evenly distributed temperature fields inside the cavity. The cavity temperature stratifications are not very high at the outer cavity (the space between the outer layer of glazing and the blinds) due to constant and isothermal boundaries. The outer cavity temperature is mostly uniform, and it is higher than the inner cavity (the space between the inner layer of glazing and the blinds). For Boundary B results, the angle between the slats and the incident beam radiation impacts the temperature fields inside the channel. It can be seen the stratification of the temperature for Boundary B does not have any noticeable order as those visible in Boundary A, especially near the blinds and the outer cavity, but for Boundary A, the inner cavity is more uniform and smooth. According to the temperature contours, almost half of the cavity is still unheated in the internal area. However, the core temperature is close to the ambient indicating that little mixing of air has taken place in the cavity's centre region (inner cavity extent).

The maximal temperatures calculated on the outlets are higher than 303 K (for Boundary A 312.76 K) and the average is higher than 300 K for both the simulations. Based on the calculation for Boundary A at the outlet, the air is heated and the temperature rise is almost 19.6 K higher than ambient temperature and for Boundary B that is 10.2 K. It looks that most of the air heated up higher than 5.9 K while extracting through the exit. For Boundary B, the maximum blind temperature reached 313.13 K, and the average value calculated is 309.14 K which is less than 1.13 K underestimation with a comparison of the measured data. And overall, Boundary A values are higher than Boundary B calculations in the domain.

3.4 Velocity fields and streamlines
DSF performance also depends on the velocity fields inside the channel. Figure 9 shows the iso-velocities inside the channel. The velocity values near the inner and outer layers and the blinds are

higher than other regions; the highest values are those shown at the exit. According to Figure 9, the flow fields looks almost the same for both the boundaries except at the higher part of (one-third from the top) the cavity. The main parameter, which causes turbulence inside the cavity, is the blinds and can be seen as a mixing zone around each blind. It might also be possible to know that there might have recirculation in the centre of the cavity. For Boundary A (Figure 9 (a)), it is clear that the velocity field is an evenly distributed velocity field with fewer air mixed zones. Both the models predicated the maximum velocity at the exit section. Boundary A calculations at the inlet and outlet are higher than Boundary B. For Boundary B, the maximum amount of velocity at the outlet about 17.5 % is underestimated compared to Boundary A results. The lowest difference between the average outlet velocity is 0.06 m/s. The average air velocity at the inlet calculated by Boundary B is slightly slower than boundary A Based on the results, both models present similar results (Boundary A values is slightly higher), thus, the streamlines figures can document specific differences between the models in the flow pattern at the top of the cavity. These can be considered insignificant for the given simulation case (same average results) but can appear critical in another case. In terms of evaluating the overall performances of the DSF related to the airflow rate and heat transfer, it might get the same results using these boundary types and average values. Streamlines are plotted to see the effect of defining the different types of boundaries on the flow structure in the studied DSF, as shown in Figure 10 (a and b). It has been tried to catch and depict the most prominent location in the cavity (one-third of topside, i.e., 1.4-2.5m from bottom), which have interestingly different flow pattern characteristics. Generally, it can be seen (Figure 10) that the flow is a boundary layer type for both types (A and B), extending along with the outer and inner layers. A complex flow field happened at the upper part of the cavity for both of the boundary conditions. In the right bottom corners of both boundary types, there are eddies of the same sizes.

Based on the studies (Giancola et al. 2018; Kalyanova et al. 2007a; Kalyanova and Heiselberg 2008; Kalyanova Larsen 2008; Larsen and Liu 2020) the information about the mass flow in the DSF cavity and conduction of experiments using the measurement methods, the flow conditions, the flow pattern in the DSF cavity, and the reverse flow are normally difficult to deal with both in modelling and experiments. Based on the references (Kalyanova Larsen 2008; Larsen and Liu 2020) it is proven that recirculation flows could appear in the wide cavities with high surface temperature but capturing the reversal flow using

CFD predictions is exceptionally rare. By reason of little studies available about the recirculating flow phenomena, it is difficult to consider how the boundary layer would develop; thus our study tried to show the flow pattern where utilizing boundary setups have been able to show this phenomenon. For Boundary A (Figure 10 (a)), the streamlines are not very distorted and almost well organized. Some small eddies are visible on the surface of each blind, and their sizes and locations are nearly the same. The airflow pattern has changed inside the cavity, accompanied by creating the secondary cells near the blinds. The size of eddies is almost the same on each blind. This would show that the heat transfer properties would be the same for each blind but the air movement from the inner layer to the outer layer follows an order until it faces a secondary eddy near the top blind. The recirculation prevents air from penetrating the blinds directly in that location. The flow concentration is mostly to the outer layer and most of the air is extracting from the middle of the outlet.

According to Figure 10 (b), for boundary B, the streamlines are not distorted very much, but the positions and the sizes of eddies along each blind do not have the same dimensions, and each one has different characteristics. This might be due to the non-uniform temperature field along with each blind.

Generally, the thickness of the boundary layers are very thin, so its effect on the flow pattern in the large spaces is insignificant but in the small spaces such as the space between the blinds, it could be effective and could affect the flow pattern dramatically. It is noted that the position of rapid changes in the flow pattern is almost the same for both methods. But the pattern of flow movement in the suddenly changed position for B is completely different from A. In the case of B, the reciprocating current moves well between the blinds, while the flow in A is unidirectional from inside to outside. The pattern of Boundary B has not been reported well in the experiments and the literature but the pattern of A is almost the same in most of the previous simulations (Fallahi et al. 2010a; Hazem et al. 2015; Iyi et al. 2014b; Ji et al. 2007a; Jiru et al. 2011b; Safer et al. 2004b; Su et al. 2017). It could be stated that this complex pattern shown in Boundary B simulations could be close to reality since the presence of the blinds are more sensible in it which previous simulations had not been able to capture.

4   Discussion
This section tries to address the main reasons for the differences between both calculations. Also,

through this, the pros and cons of each boundary type are clarified well.

For Boundary B, the angle between the slats and the incident beam radiation impacts the channel's temperature fields as the radiation is the primary heat source. The temperature of the blinds and the glass surfaces in Boundary B is not uniform and the surfaces are not isothermal. This is the result of the solar heat flux applied to the domain for boundary B, which causes non-uniform surface heat flux on glazing and blinds. Therefore, the calculation of the velocity and airflow pattern inside the cavity for this type of solution is also different from Boundary A. As shown (Figures 6-12), the main differences between the simulations are likely related to the local values and the simple assumption of uniform surface temperatures used in applied in Boundary A; Boundary B predicts the blind's temperature differently from the bottom to the top but on the surfaces of each blind, so we do not have a constant temperature field at all; when the temperatures are calculated differently and higher than the other types or the real values, it means that there is a heat source in the cavity differently (in type B compared to A). This would also mean that we might see more pronounced differences between A and B cases for a higher solar load than the described case. These differences will also be very remarkable in fluid motion and to better prediction of temperature and velocity profile.

According to the simulation results, the most significant difference between the models is the airflow rate; the flow pattern and temperature differences are not as pronounced as the airflow rate. As a finding, it should be discussed more. The surface temperatures of both models were calculated differently and these differences had their effect on the thermal and flow fields directly. The values calculated by Boundary B are lower than Boundary A.

To clarify the origin of these differences we have to conduct further investigations considering the low temperature/flow values of Boundary B comparing Boundary A; thereby the value of heat fluxes through the outer/inner layers were also evaluated; Referring to the literature (Zhang and Yang, 2019b; Kimouche, 2017) the energy input to the cavity has a great impact on the evolution of the convection resulting increasing temperature and velocity in the naturally ventilated cavities. Based on the simulations, the heat flux through the outer layer for Boundary B is almost 25% lower than Boundary A which would indicate lower temperature rise and consequently lower velocity field due to lowering buoyant forces inside the cavity (Kalyanova and Heiselberg 2008; Kalyanova

Larsen 2008) reduced heat flux (through the outer layer) could be discussed using two main standpoints. First, from the simulation standpoint, the reduction could be related to how DOM deals with solving radiative transport equations. It was discussed (look Boundary B descriptions section) that the DOM contains two main numerical errors (known as ray effect or ray concentration and false scattering) which must be alleviated before the simulation. In the literature it was suggested to alleviate the errors through increasing the control angle count, increasing the spatial mesh count, and; using a higher-order spatial discretization scheme for the DOM direction equation (Moghimi et al.2015, 2016, Craigh et al.2016). The ray effect error would generate a wavy solution in heat flux calculations that affects mapping the non-uniform solar heat flux load on the surfaces. This could be alleviated by the mentioned methods somehow but considering their implementation in ANSYS-Fluent due to its closed-source specification is almost impossible (Moghimi et al. 2015). Thus a complete tackling of the error based on the available processing hardware is inevitable to some extent. From the modelling standpoint, it should be stated that according to the domain modelling approach (isolation method in this case), it is only possible to implement the irradiation boundary conditions offered by DOM on the solid surfaces rather than whole outdoor faces of DSF (i.e. the inlet and outlet areas - the area in 2D implies as the length of the boundary- have been excluded form determination of incoming solar heat flux) and this could be considered as a limitation of Boundary B method (see Figure 3). The arrows in Figure 3 exactly depict the area where the irradiation could be implemented into the domain. The reduced flux (combining with the ray effect error) would affect the total energy coming to the domain and it significantly affects the induced air flow rate and the average temperature rise. Improvements in these two parameters may result in a straight increase in the flow rate and the temperature rise, as the energy input of the flow and heat transfer greatly improves. The modelling related shortage could be solved by modelling openings in the floor and ceiling instead of façade. So all these could cause the values were predicted for Boundary B to be less than Boundary A and be the reason for the intensification of the airflow differences between the two calculations.

Given the prediction results at the regarded points in Figure 6 and Figure 7, almost every simulation presents an unacceptable error for that point. The airflow comes through the Venetian blind from the inner part of DSF to the outer part, and point four (middle point) is the closest to the blind. It means that if the air velocity is measured 0.01 m higher or lower, the values can change considerably.

The thermal boundary might be the reason for the discrepancy between measured and simulated results; the other, boundary setup or numerical model (for example turbulence model or radiation model) also cause the discrepancies. Also, the discrepancies might be due to the measurement uncertainties and available rough data that is, temperature and velocity measurements especially under solar exposure in the given range is not easy to conduct (Kalyanova et al. 2007a; Kalyanova et al. 2007b). Thus the discrepancies between the measurement and simulations are not avoidable and can be caused both by simulations and inaccurate measurements. Thus, it not only important to look at the absolute values, but also it is necessary to look at the trends within the measured parameters. The detailed measurement results are still missing and this will cause difficulty in the validation.

With regards to flow pattern (Figure 10) it was shown that the presence of the blinds in Boundary B results are more sensible and the flow is more complex than Boundary A. The fact that this complexity has not been shown before does not mean that it is wrong; it simply means more investigation is needed to conclude on it. However, we must acknowledge that Boundary B can address the complexity of solar radiation- boundary conditions, which can be critical for modelling of blinds and thereby Boundary B has the potential to better capturing the airflow of DSF. For a valid judgment, it is necessary to observe the real phenomena in real setups using highly accurate experimental measurements.

To sum up, although the observable differences can be found between the numerical and experimental results, the changing tendencies and patterns are similar at the given heights of the channel for the boundary types (A and B). Based on the current capacities provided by Boundary B, it could be an excellent choice for the simulation of DSFs in a way that Boundary B can give more possibilities in defining more types of boundary conditions simultaneously, controlling more parameters such as irradiation intensity, incidence angle, and outdoor/indoor weather conditions. It could be considered that very complex geometries are possible to study using Boundary B.

It should be said that the important parameters are not the ones with differences, but once that matter for the overall evaluation of performance. For example, the different velocities on the surface could affect other parameters such as the convective heat transfer coefficient. The effect of the consequences of the differences on the temperature and velocity in the vertical cross-section of the cavity is presented and discussed in the following.

4.1 Vertical section results of temperature and velocity for Boundary A-B

The vertical sections of DSF in the cavity were plotted to see and discuss how temperature and velocity would be affected by the sudden change of pattern between the blinds using defined boundary conditions. In Figure 11, the velocity profile and temperature distributions are plotted in the vertical cross-sections at three different positions (x=0.062 m - 0.05 m near the outer glass, x=0.275 m - middle of the cavity, x=0.512 m - 0.05 m from near inner glass). Figure 11 shows the temperature distribution tendency for both types of boundary conditions is very similar, yet the temperature calculations for boundary B are lower than boundary A in all cross-sections. The calculated average temperature for Boundary A is 296.91 K. This value for Boundary B is 296.67 K which shows that the average temperature difference is less than 0.24 K. The maximal temperature difference between two boundary types A and B is less than 4 K. As seen in the centre of DSF (x=0.287 m), there is a bump at the top of the DSF (from 1.5 m to 2.5 m height) where the flow pattern has been distorted. This would show that there is a very sudden change in the velocity magnitude and directions.

Figure 12 depicts the velocity profile at three cross-sections for both types of boundary conditions. The velocity profile in the cross-section near the inner glass for Boundary B compared against Boundary A, illustrates that the solar heat gain distribution between the sub-cavities is not alike. The oscillations for Boundary B are more pronounced, in particular, near the outer glass and the blinds. Without direct solar radiation (Boundary A), the velocity profile is much more uniform, and the airflow is concentrated in the outer part of the channel. According to Figure 12, the velocity magnitude at the vertical sections is very variable near the outer layer. The vertical position (1.5 m to 2.5 m from the bottom) is a very critical location in a way that the performance of DSF is going to be unpredictable. Although the simulation is steady, after doubling the iteration times the flow pattern was changing consequently for both the boundary types which changing the pattern for Boundary B was apparent than Boundary A. There is also a bump of change in velocity at the position of 1.5 m to 2 m height exactly where the temperature distributions had rapid differences (Figure 11). This change would show the reason for the low temperature on the blinds in the Boundary B simulation. For example in Boundary B, in the middle of the cavity at 2m height from the bottom, the velocity value is higher than Boundary A and its direction is also different; this caused the enhancement of heat transfer rate on the blinds resulting in reducing the temperature on the

regarded location (look at Figure 8) but this pattern is not shown in Boundary A simulations. Overall the main reasons for the difference between both the simulations are likely related to the local non-uniform temperature calculations of the Boundary B compared with the constant temperature of Boundary A.

According to literature (Kalyanova and Heiselberg 2008; Kalyanova Larsen 2008), little attention was paid to the surface temperatures in the cavity and the experiment room, since these are entirely dependent on the surface film coefficients. Referring to the reference (Kalyanova Larsen 2008; Oesterle 2001), it was shown that the surface temperature of the glazing was identical for all windows in the same pane measured on; thus the different surface temperatures would cause the main differences in the flow regime, air velocity and temperature between both the models. In order to evaluate the reason and basis of the observed differences between the calculations, it is worth assessing the surface temperatures on the inner and outer layers in detail to see how both the models dealt with it. Figure 13 shows the vertical temperature gradients inside the cavity for Boundary A and B. This also would show the implementation of the different assumptions in the thermal boundary conditions of Boundary A with assumed uniform temperature compared to Boundary B. Based on Boundary B simulation the glass surface temperature increases compared to the outdoor air temperature (293.15 K) with presenting of the solar radiation, due to the absorption. Regardless of the differences between the surface temperatures of A and B, it is seen that the surface temperature of the glazing and blinds in Boundary B presents variations locally with the height of the cavity; there happens a temperature reduction at the upper and lower parts of the inner layer (at the inlet/outlet extents) due to absence of the solar irradiation modelling resulted from Boundary B modelling limitation which was discussed in the previous section (see Figure 3). This also implies the fact that the glass surface temperates are sensitive to the modelled solar irradiation by the DOM compared to the constant surface temperature of model A. The surface temperature of Boundary A is higher than Boundary B and these high surface temperatures result in a strong boundary layer flow compared to each other. This would also affect the flow rates and related extracted heat significantly.

4.2 Comparison of the calculated average values for Boundary A and B

Simulation results showed that local values differed for both types of boundary conditions, so it's worth seeing how other average values are calculated for both cases. The cavity has a low mean air velocity of less than 0.2 m/s, and the Reynolds number has an order of $1*10^4$-$2.5*10^4$. Table 7 summarizes the corresponding variables for each type of boundary condition. The Boundary A results are generally higher than Boundary B. Although there are differences among the results, the order of differences is insignificant. The evaluation of the DSF performance was not in the interest of the paper, but through both the utilized approaches it is possible to conduct such a study. One of the important functions of DSF is to enhance the ventilation of the cavity by extracting the air from the inside by equipped openings. The results presented that the air temperature rise through the cavity could reach up to 5.15 K, and the induced airflow rate varied in the region of 234–273 m^3/h (115-134 ach). Thus, this heated air could be transferred to the inside via airflow from the operable inner layer for winter function, but having calculated flow rate and temperature differences, the studied cavity could transfer the heated air to the outside during summer function.

It is also possible to end this discussion if local values are not important for studying and instead the average values are considered, and then there is not much sensitivity in choosing between two different boundary conditions.

5 Conclusion

A CFD model for the naturally ventilated DSF was developed. This work's scope was to show what type of boundary conditions is suitable for modelling naturally-ventilated DSF study. Thus, this study provided information for developing and selecting an appropriate DSF system simulation using CFD. Two different types of boundary conditions (called A and B types) were applied for a unique naturally ventilated DSF.

Boundary B includes more complex and more equations to solve (continuity, momentum, energy, and RTE solved using DOM) than Boundary A. Therefore, Boundary B takes more time to solve (almost 3.7 times higher) and it needs much effort to set up the model from the first step of the simulation process.

The temperature distribution at the middle height of DSF is nearly the same and both the models followed a similar trend of variations. Looking upon air velocity calculations at the middle height of the cavity and based on the point by point comparison of the results with the measurements, it was seen that Boundary B had better predictions than Boundary A. However, that was Boundary A which could predict temperature well at the middle height of the cavity. Here, the authors acknowledge

uncertainties related to the limited experimental data and the lack of its accuracy evaluation.

Based on streamlines in the vertical section of the cavity, the mixing of air between two sub-cavities is distinct only for boundary B than Boundary A. It could be argued that this complex pattern is close to the reality in which the presence of the blinds are considered in Boundary B simulation since there are shown that air recirculates and passes through the blinds clearly but this pattern could not be captured in Boundary A. In this regard, more investigations are needed to conclude on it and for a valid judgment which is necessary to observe the real phenomena using an experimental study.

Overall, comparing the results of the two types of boundary conditions, it was found that there are many differences between the local data, while the results of the average values are close. The boundary B approach allows the assessment of DSF elements with an integrated shading device without knowledge of the surface temperatures, particularly the Venetian blinds' temperature. It also offers a possibility to model complex geometries, including self-shading and similar passive approaches. All of the mentioned features could be possible through only using a single computational and numerical tool. Furthermore, it has the potential of capturing the mixing air between the sub-cavities, which can be crucial for conditions with higher incident solar radiation than the ones considered in this study. In both the boundaries type, the airflow from the inlet to the outlet was shown smoothly. Consequently, the performance of the DSF in ventilation and removing heat from the cavity were confirmed by our results. The study could be a starting point for evaluations of the different types of boundary condition settings and also defining new experimental studies in this regard.

Appendix A. Supplementary material
Figure 14 shows the comparison of the current study temperature simulation at the middle height of the cavity with previously published studies done by Iyi et al.(2014) and Pasut and Carli (2012) and Ji et al. (2007). The comparison indicates that this range of difference between measurements and CFD simulations has been reported already. Also, our results have shown a very negligible difference with the mentioned studies and the values at the regarded points predicated with a similar range. The thermal boundary might be one of the reasons for the discrepancy between measured and simulated results, the other reason might be linked to boundary setup or numerical model (for example turbulence model or radiation model) which caused the discrepancies. Besides, Kim (2020) used Mei et al.2007 to validate his model, and the author linked

the discrepancies to the experimental uncertainty. Thus the discrepancies more likely due to the available rough experiment data that is, detailed measurement results are still missing and this will cause difficulty in the validation for the researchers. Through Figure 14, it is possible to compare our study results and the previous studies clearly.

6 References

Agathokleous RA, Kalogirou SA (2016). Double skin facades (DSF) and building integrated photovoltaics (BIPV): A review of configurations and heat transfer characteristics. Renewable Energy, doi:10.1016/j.renene.2015.12.043.

Anđelković AS, Gvozdenac-Urošević B, Kljajić M, Ignjatović MG (2015). Experimental research of the thermal characteristics of a multi-storey naturally ventilated double skin façade. Energy and Buildings, doi:10.1016/j.enbuild.2014.11.007.

ANSYS Inc (2016). Fluent. Ansys. Available at https://www.ansys.com/products/fluids/ansys-fluent.

Barbosa S, Ip K (2014). Perspectives of double skin façades for naturally ventilated buildings: A review. Renewable and Sustainable Energy Reviews, doi:10.1016/j.rser.2014.07.192.

Belgian Building Research Institute (2020). Source Book for a Better Understanding of Conceptual and Operational Aspects of Active Facades. Belgium: Department of Building Physics.

Betts PL, Bokhari IH (2000). Experiments on turbulent natural convection in an enclosed tall cavity. International Journal of heat and fluid Flow, 21: 675–683.

Chen Q, Srebric J (2002). A procedure for verification, validation, and reporting of indoor environment CFD analyses. HVAC&R Research, 8: 201–216.

Coussirat M, Guardo A, Jou E, Egusquiza E, Cuerva E, Alavedra P (2008). Performance and influence of numerical sub-models on the CFD simulation of free and forced convection in double-glazed ventilated façades. Energy and Buildings, 40: 1781–1789.

Craig KJ, Moghimi MA, Rungasamy AE, Marsberg J, Meyer JP (2016). Finite-volume ray tracing using Computational Fluid Dynamics in linear focus CSP applications. Applied Energy, 183: 241–256.

Darkwa J, Li Y, Chow D (2014). Heat transfer and air movement behaviour in a double-skin façade. Sustainable Cities and Society, doi:10.1016/j.scs.2013.07.002.

Desrayaud G, Chénier E, Joulin A, Bastide A, Brangeon B, Caltagirone JP, Cherif Y, Eymard R, Garnier C, Giroux-Julien S, Harnane Y, Joubert P, Laaroussi N, Lassue S, Le Quéré P, Li R, Saury D, Sergent A, Xin S, Zoubir A (2013). Benchmark solutions for natural convection flows in vertical channels submitted to different open boundary conditions. International journal of thermal sciences, doi:10.1016/j.ijthermalsci.2013.05.003.

Fallahi A, Haghighat F, Elsadi H (2010). Energy performance assessment of double-skin façade with thermal mass. Energy and Buildings, 42: 1499–1509.

Gaillard L, Giroux-Julien S, Ménézo C, Pabiou H (2014). Experimental evaluation of a naturally ventilated PV double-skin building envelope in real operating conditions. Solar Energy, 103: 223–241.

Gan G (2006). Simulation of buoyancy-induced flow in open cavities for natural ventilation. Energy and Buildings, doi:10.1016/j.enbuild.2005.08.002.

Gavan V, Woloszyn M, Roux J-J, Muresan C, Safer N (eds) (2007). An investigation into the effect of ventilated double-skin facade with venetian blinds: Global simulation and assessment of energy performance.

Giancola E, Sánchez MN, Friedrich M, Larsen OK, Nocente A, Avesani S, Babich F, Goia F (2018). Possibilities and challenges of different experimental techniques for airflow characterisation in the air cavities of façades. Journal of Facade Design and Engineering, 6: 34–48.

Gracia A de, Navarro L, Castell A, Cabeza LF (2015). Energy performance of a ventilated double skin facade with PCM under different climates. Energy and Buildings, doi:10.1016/j.enbuild.2015.01.011.

Gratia E, Herde A de (2004). Natural ventilation in a double-skin facade. Energy and Buildings, doi:10.1016/j.enbuild.2003.10.008.

Guardo A, Coussirat M, Egusquiza E, Alavedra P, Castilla R (2009). A CFD approach to evaluate the influence of construction and operation parameters on the performance of Active Transparent Facades in Mediterranean climates. Energy and Buildings, 41: 534–542.

Guardo A, Coussirat M, Valero C, Egusquiza E, Alavedra P (2011). CFD assessment of the performance of lateral ventilation in Double Glazed Façades in Mediterranean climates. Energy and Buildings, 43: 2539–2547.

Hazem A, Ameghchouche M, Bougriou C (2015). A numerical analysis of the air ventilation management and assessment of the behavior of double skin facades. Energy and Buildings, 102: 225–236.

Hiroyuki O, Hayatoshi S, Churchill SW (1974). Natural convection in an inclined square channel. International Journal of Heat and Mass Transfer, 17: 401–406.

Ibañez-Puy M, Vidaurre-Arbizu M, Sacristán-Fernández JA, Martín-Gómez C (2017). Opaque Ventilated Façades: Thermal and energy performance review. Renewable and Sustainable Energy Reviews, 79: 180–191.

Iyi D, Hasan R, Penlington R, Underwood C (2014). Double skin façade: Modelling technique and influence of venetian blinds on the airflow and heat transfer. Applied Thermal Engineering, 71: 219–229.

Ji Y, Cook MJ, Hanby, V I, Infield, D G, Loveday, D L, Mei L (eds) (2007). CFD modeling of Double-Skin-Facades with Venetian Blinds. Salford University, Manchester. Available at http://usir.salford.ac.uk/15842/. Accessed 9 Jan 2020.

Jiru TE, Tao Y-X, Haghighat F (2011). Airflow and heat transfer in double skin facades. Energy and Buildings, 43: 2760–2766.

Kalyanova Larsen O (2008). Double-Skin Facade: Modelling and Experimental Investigations of Thermal Performance, Ph.D. Thesis, Department of Civil Engineering, Aalborg University. Denmark. Available at https://vbn.aau.dk/ws/portalfiles/portal/3164 20577/Double-Skin_Facade. Accessed 2020.

Kalyanova O, Heiselberg P (2008). Empirical Validation of Building Simulation Software: Modelling of Double Facades: Final Report: Technical Report: IEA ECBCS Annex 43/SHC Task 34-Validation of Building Energy Simulation Tools: Subtask E. Aalborg University, Department of Civil Engineering.

Kalyanova O, Jensen RL, Heiselberg P (eds) (2007a). Measurement of air flow rate in a naturally ventilated double skin façade. Proceedings of Roomvent 2007. Finland: FINVAC ry.

Kalyanova O, Zanghirella F, Heiselberg P, Perino M, Jensen RL (2007b). Measuring air temperature in glazed ventilated facades in the presence of direct solar radiation. I: Proceedings of Roomvent 2007. Finland: FINVAC ry.

Kim DD (2020). Computational fluid dynamics assessment for the thermal performance of double-skin façades in office buildings under hot climatic condition. Building Services Engineering Research and Technology, 0143624420952962.

Kim SY, Song KD (2007). Determining photosensor conditions of a daylight

dimming control system using different double-skin envelope configurations. Indoor and Built Environment, 16: 411–425.

Kimouche N, Mahri Z, Abidi-Saad A, Popa C, Polidori G, Maalouf C (2017). Effect of inclination angle of the adiabatic wall in asymmetrically heated channel on natural convection: Application to double-skin façade design. Journal of Building Engineering, 12: 171–177.

Kiwan S, Khodier M (2008). Natural convection heat transfer in an open-ended inclined channel-partially filled with porous media. Heat Transfer Engineering, 29: 67–75.

Kuznik F, Catalina T, Gauzere L, Woloszyn M, Roux J-J (2011). Numerical modelling of combined heat transfers in a double skin façade–Full-scale laboratory experiment validation. Applied Thermal Engineering, 31: 3043–3054.

Larsen OK, Liu M (2020). 9 Computational performance prediction of Double-Skin Ventilated Facade. Building Performance Simulation and Characterisation of Adaptive Facades–Adaptive Facade Network, 89.

Manz H (2003). Numerical simulation of heat transfer by natural convection Numerical simulation of heat transfer by natural convection in cavities of facade elements. Energy and Buildings, 35: 305–311.

Mei L, Loveday D, Infield D, Hanby V, Cook M, Ji Y, Holmes M, Bates J (2007). The influence of blinds on temperatures and air flows within ventilated double-skin façades. Proceedings of Clima 2007 WellBeing Indoors.

Moghimi MA, Craig KJ, Meyer JP (2015). A novel computational approach to combine the optical and thermal modelling of Linear Fresnel Collectors using the finite volume method. Solar Energy, doi:10.1016/j.solener.2015.04.014.

Moghimi MA, Rungasamy A, Craig KJ, Meyer JP (eds) (2016). Introducing CFD in the optical simulation of linear Fresnel collectors. AIP Publishing LLC.

Oesterle E (2001). Double skin facades: Integrated planning; building physics, construction, aerophysics, air-conditioning, economic viability. Prestel.

Ospir D, Popa C, Chereches C, Guillaume, Polidori, Fohanno, Stéphane (2012). Flow visualization of natural convection in a vertical channel with asymmetric heating, doi:10.1016/j.icheatmasstransfer.2012.02.005.

Pasut W, Carli M de (2012). Evaluation of various CFD modelling strategies in predicting airflow and temperature in a naturally ventilated double skin façade. Applied Thermal Engineering, 37: 267–274.

Poizaris H (2004). Double skin facades for office buildings: Literature review. Tech. Rep.

Pomponi, Francesco; Poorang A.E. Piroozfar, Ryan Southall, Philip Ashton, Eric. R.P. Farr (2016). Energy performance of Double-Skin Façades in temperate climates_ A systematic review and meta-analysis.

Safer N, Woloszyn M, Roux JJ (2005a). Three-dimensional simulation with a CFD tool of the airflow phenomena in single floor double-skin facade equipped with a venetian blind. Solar Energy, 79: 193–203.

Safer, N., Gavan, V., Woloszyn, M. and Roux, J.J., (2006). Double-skin façade with Venetian blind: global modelling and assessment of energy performance. In EPIC Conference, Lyon (France).

Safer, N., Woloszyn, M., Roux, J. J., & Kuznik, F. (2005b). Modeling of the double-skin facades for building energy simulations: radiative and convective heat transfer. In 9th International IBPSA Conference Building Simulation (Vol. 2): 1067-1074.

Safer, Nassim; Woloszyn, Monika; Rusaouën, Gilles; Roux, Jean Jacques (Eds.) (2004): Numerical studies with CFD approach of the heat and air flow transfers combined with solar radiation in double skin facades. The 21th conference on passive and low energy architecture. Eindhoven, The Netherlands: Plea2004, checked on 1/8/2020.

Su Z, Li X, Xue F (2017). Double-skin façade optimization design for different climate zones in China. Solar Energy, 155: 281–290.

Wu T, Lei C (2015). On numerical modelling of conjugate turbulent natural convection and radiation in a differentially heated cavity. International Journal of Heat and Mass Transfer, 91: 454–466.

Yuan, J., & Srebric, J. (2004). Transient prediction of contaminant distribution by introducing energy load calculations into multi-zone modeling. In CIB World Building Congress 2004 (pp. 2-7).

Zeng Z, Li X, Li C, Zhu Y (2012). Modeling ventilation in naturally ventilated double-skin façade with a venetian blind. Building and Environment, doi:10.1016/j.buildenv.2012.04.007.

Zhai Z, Chen, Qingyan, Klems, Joseph H, Haves P (2008). Principles and Strategies on Coupling Energy Simulation and Computational Fluid Dynamics Programs.

Zhang T, Chen Q (2007). Novel air distribution systems for commercial aircraft cabins.

Building and Environment, doi:10.1016/j.buildenv.2006.02.014.

Zhang T, Yang H (2019a). Flow and heat transfer characteristics of natural convection in vertical air channels of double-skin solar façades. Applied Energy, doi:10.1016/j.apenergy.2019.03.072.

Zhang T, Yang H (2019b). Flow and heat transfer characteristics of natural convection in vertical air channels of double-skin solar façades. Applied Energy, 242: 107–120.

Zöllner A, Winter ER, Viskanta R (2002). Experimental studies of combined heat transfer in turbulent mixed convection fluid flows in double-skin-facades. International Journal of Heat and Mass Transfer, 45: 4401–4408.
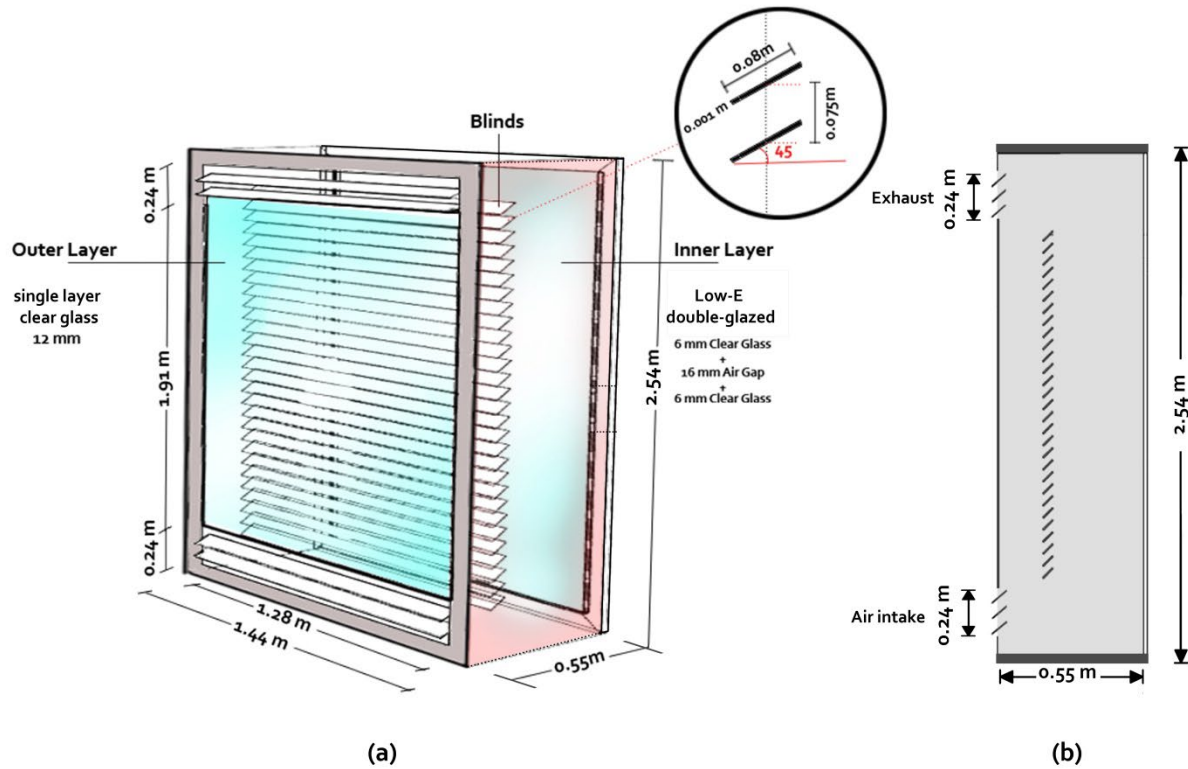
Figure 1. The dimension of the DSF of Mei et al. study (Mei et al.2007): (a) the perspective view and dimensions, (b) section view.
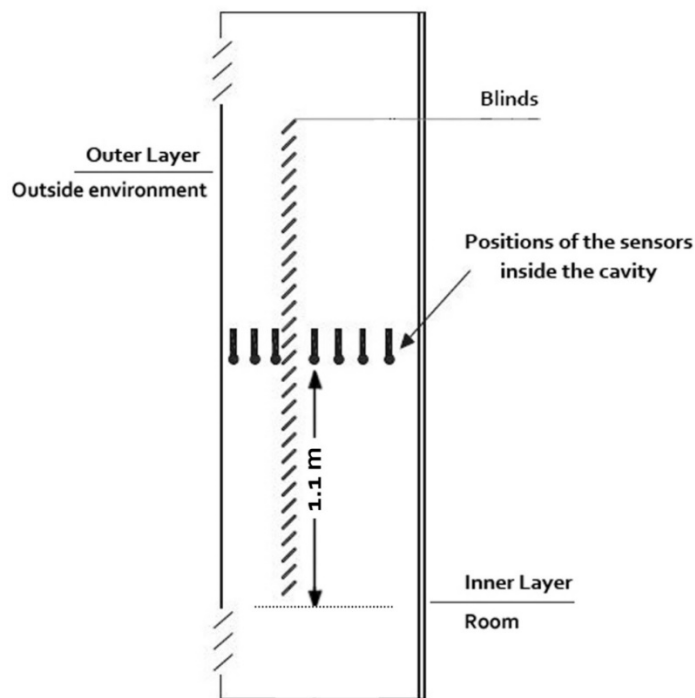
Figure 2. Location of installed temperature and velocity sensors
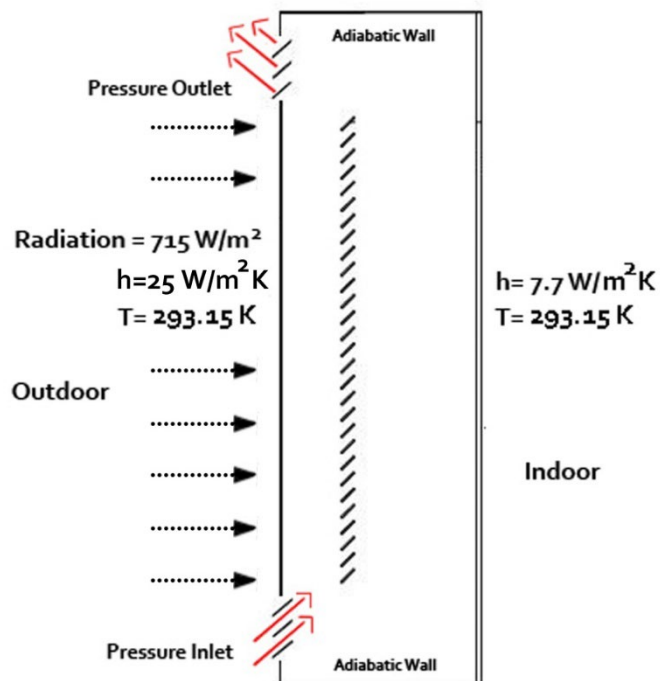
Figure 3. Regarded boundary conditions settings for Boundary B

15
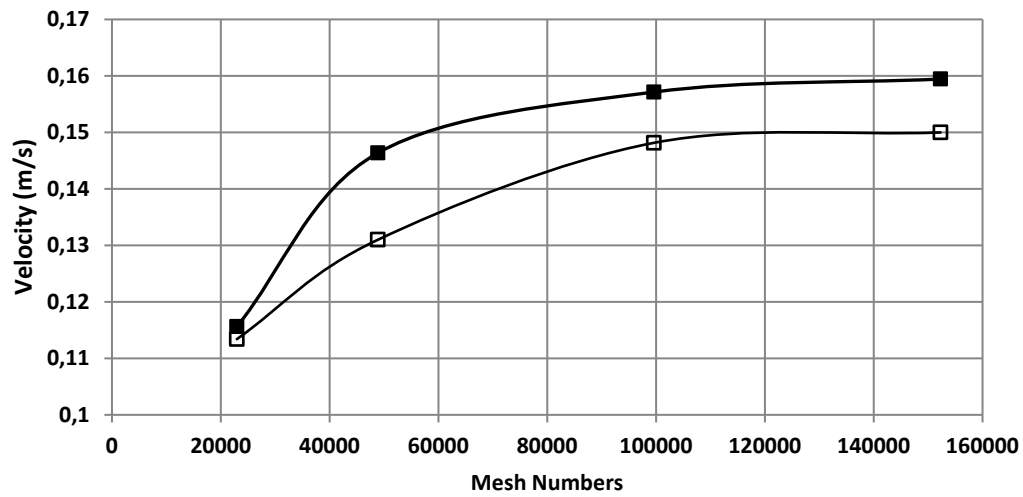
(a)
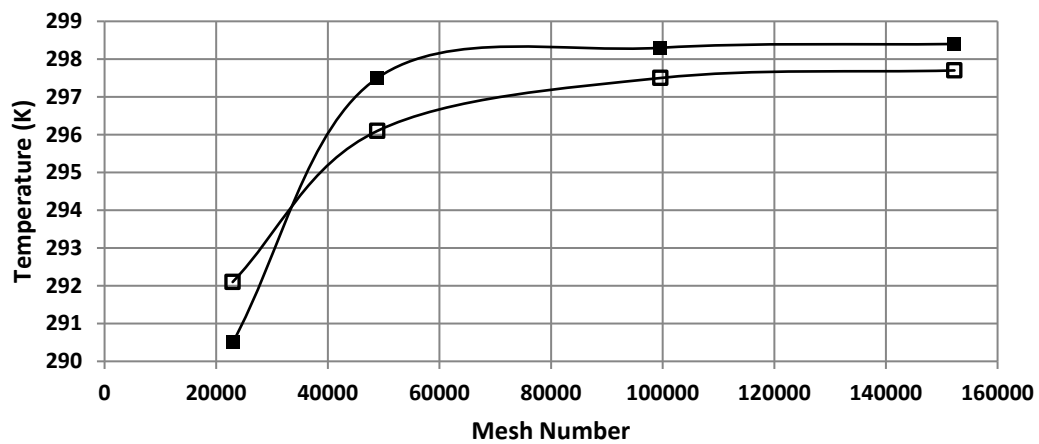
(b)

Figure 4. Mesh independence test: (a) Average cavity air velocity at the middle height of the cavity for both Boundary A and B; (b) Average cavity air temperature of Boundary A-B for mesh independence test

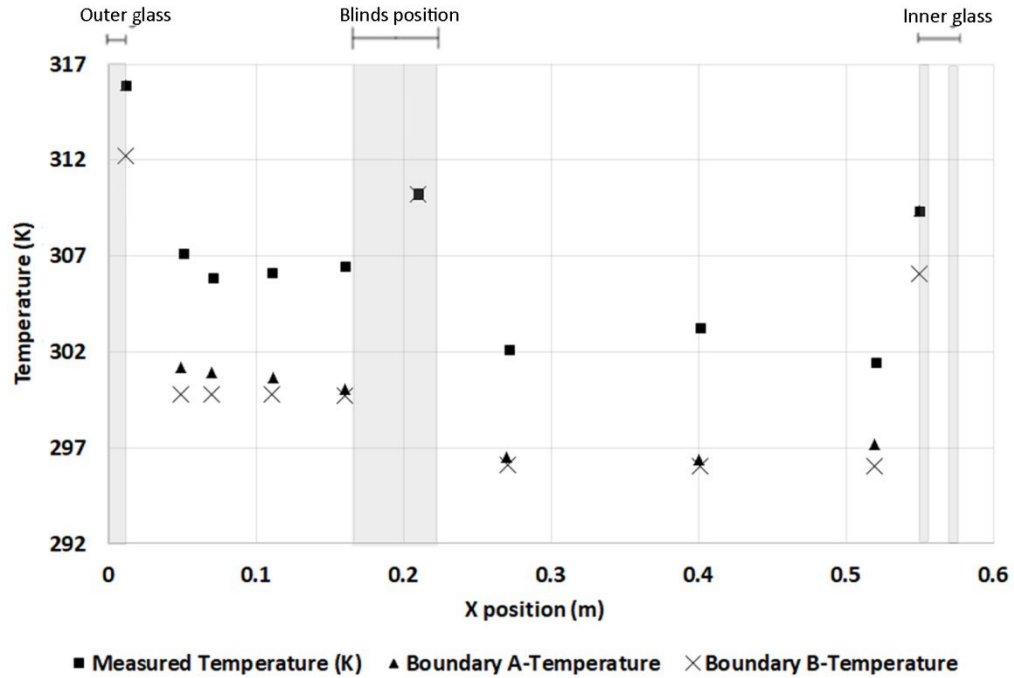16
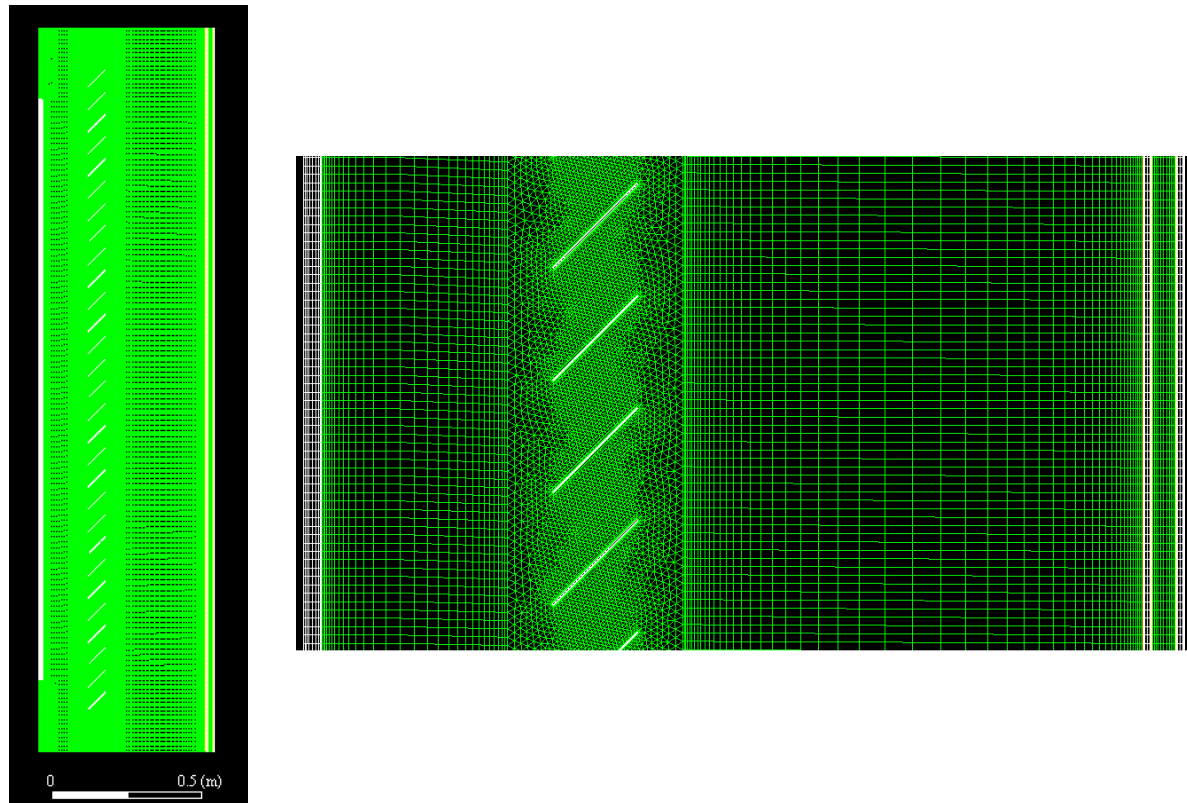
Figure 5. Hybrid meshing used for the simulations (Fine mesh)

Figure 6. Temperature distributions at the middle height of DSF (1.11m from bottom) for both Boundary A and B in comparison with experimental data
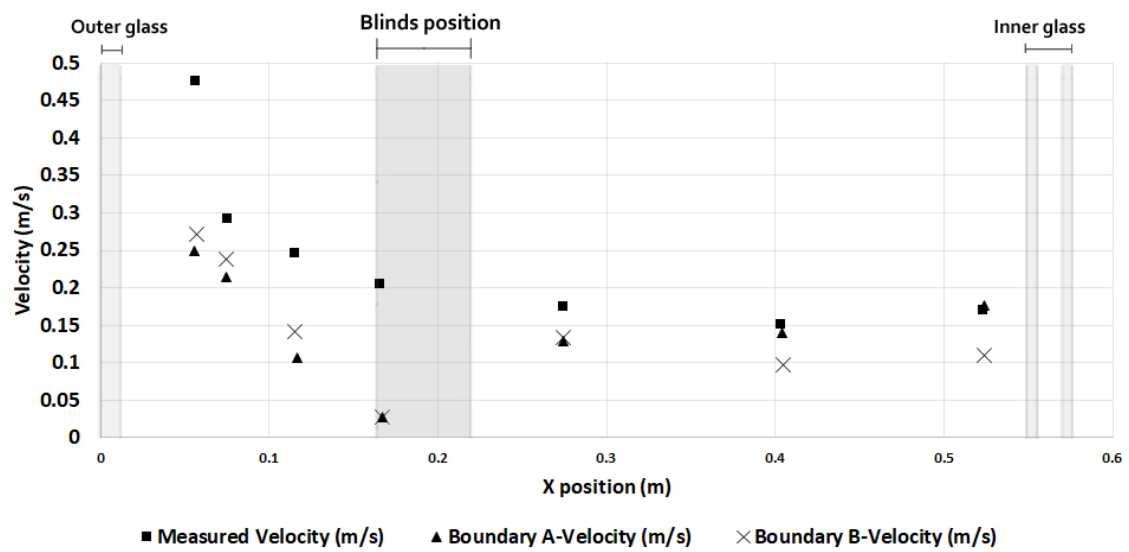
Figure 7. Velocity profile at the middle height of DSF (1.11m from bottom) for both Boundary A and B in comparison with experimental data

	323.15
	321.00
	318.86
	316.72
	314.57
	312.43
	310.29
	308.15
	306.00
	303.86
	301.72
	299.57
	297.43
	296.83
	296.50
	296.41
	295.29
	293.15

Temperature (K)

a) Boundary A   b) Boundary B
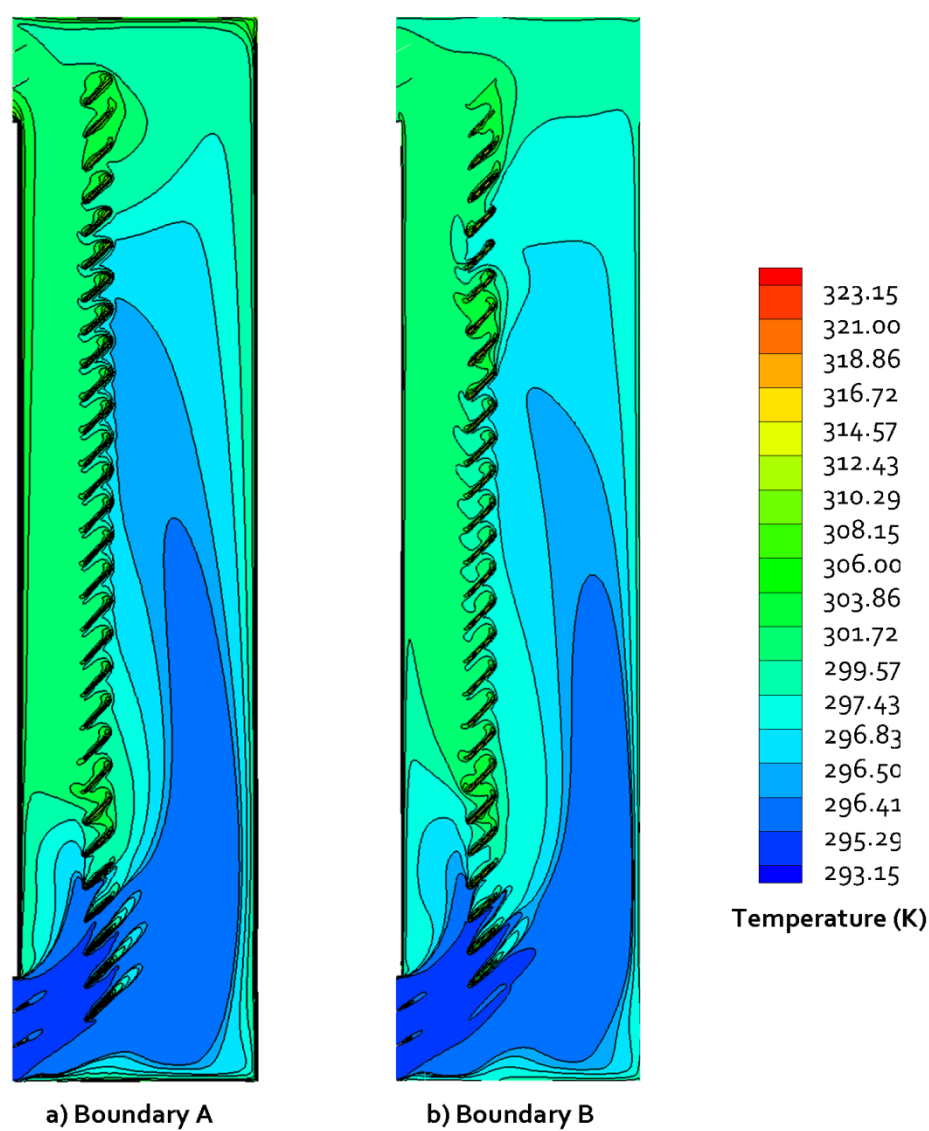
Figure 8. Temperature distributions: a) Boundary A, b) Boundary B
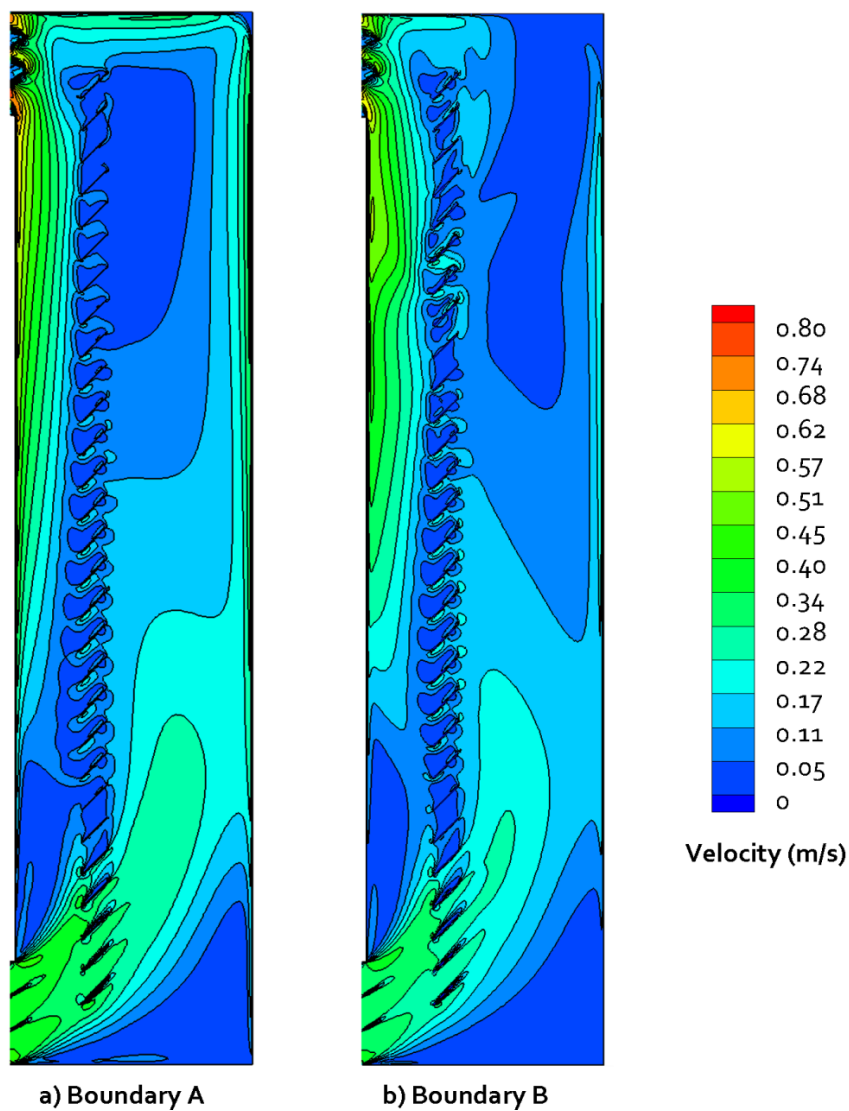
Figure 9. Iso-velocities inside the channel for Boundary A (a) and Boundary B (b)

a) Boundary A
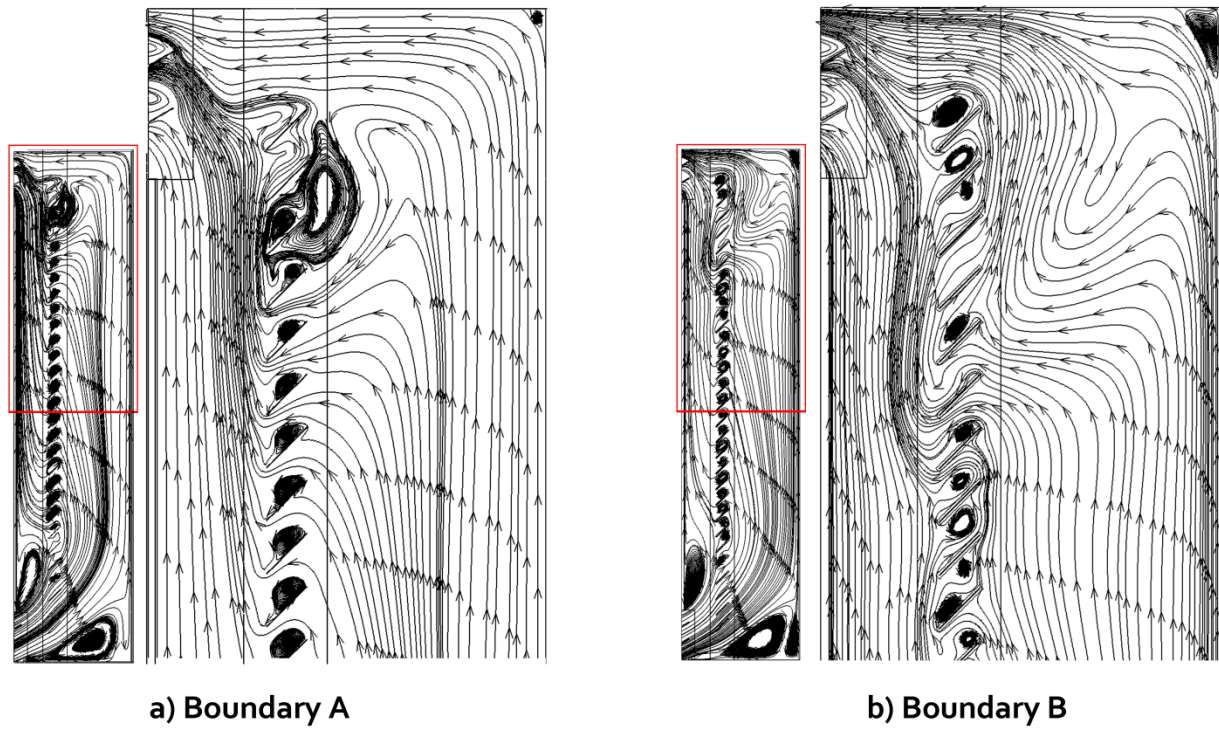
b) Boundary B

Figure 10. Streamlines for Boundary A (a) and Boundary B (b)

Boundary A (0.05 m from outer glass)
Boundary B (0.05 m from outer glass)

Boundary A (x=0.287 m-middle of cavity)
Boundary B (x=0.287 m-middle of cavity)

Boundary A (0.05 m from inner glass)
Boundary B (0.05 m from inner glass)
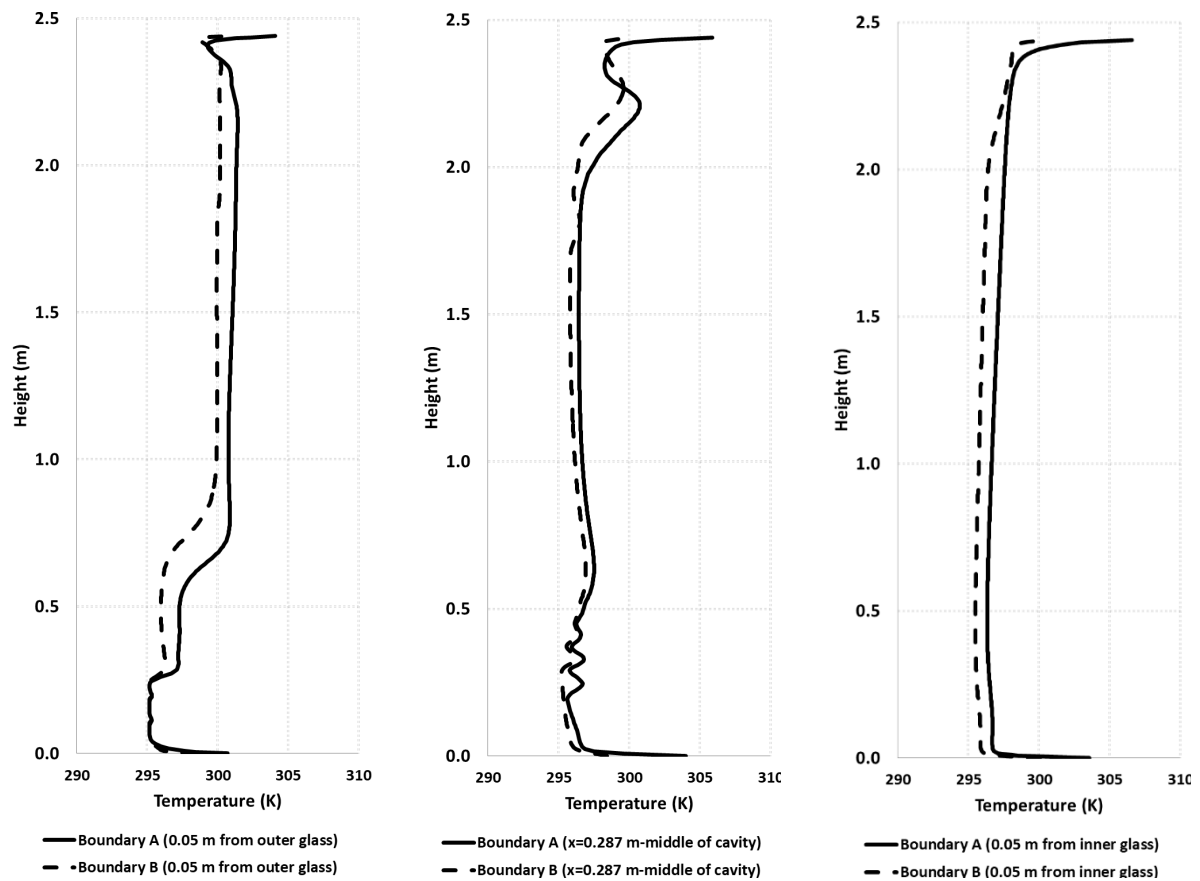
Figure 11. Temperature distribution for three cross-sections of the cavity for Boundary A and B

21
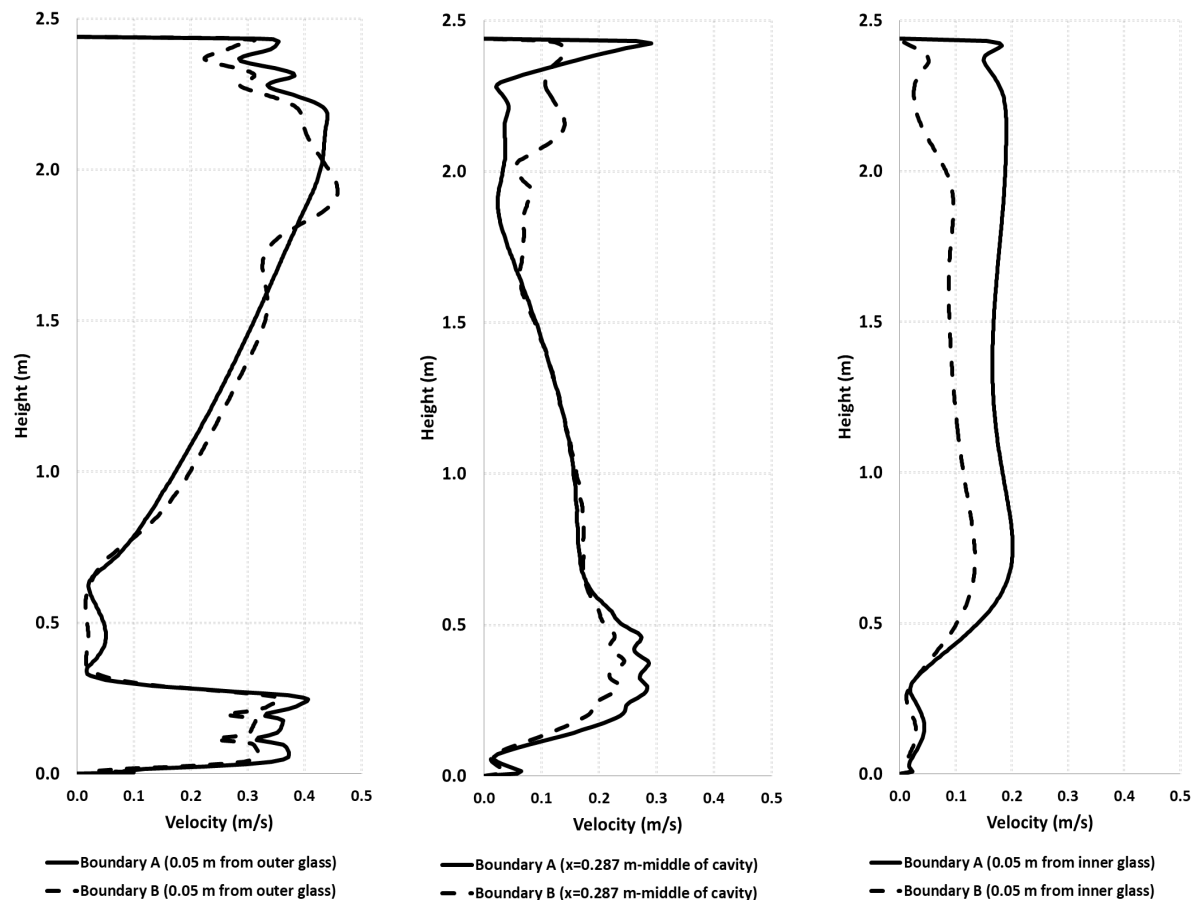
Figure 12. Velocity profiles along the channel placed at three different widths of the DSF for Boundary A and B
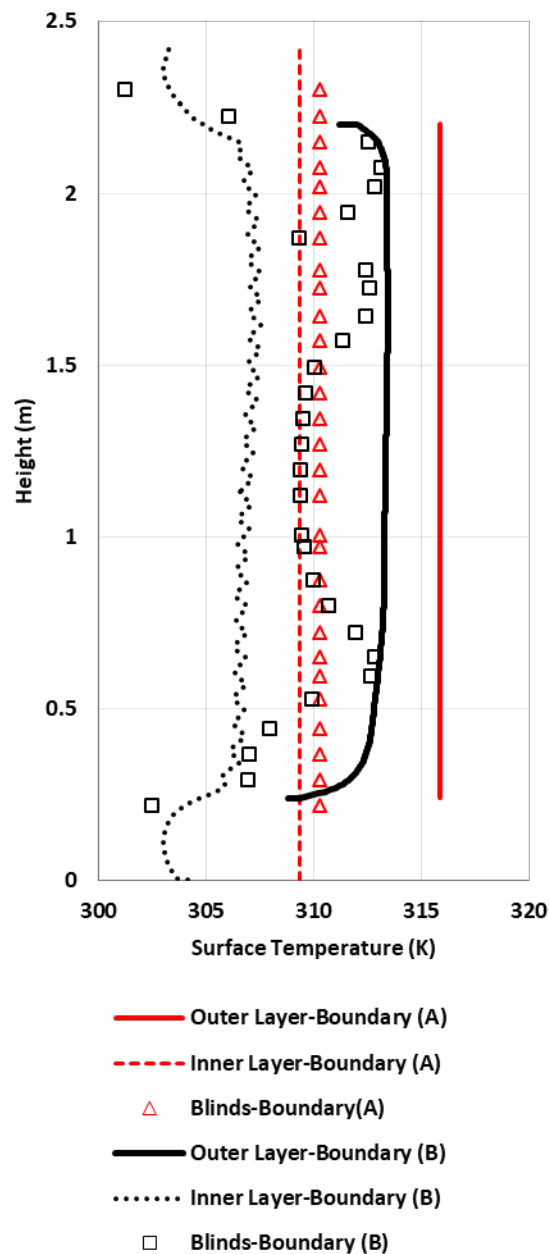
Figure 13. Vertical gradient temperature on inner, outer layer and blinds for Boundary A and B.

Table 1. All considered assumptions for the cases

Geometry Modeling Technique	Isolated DSF
Environment	2D Simulation
Solver	Pressure Based
Scheme	Steady-state
Density	Density = Boussinesq Approximation

Turbulent Model	K-e RNG, Enhanced wall treatment (for wall function) $Y+ \leq 1$ (calculated y=0.00021 m)
Discretization methods	Body force weighted for pressure discretization method
	Second-order for the rest of the discretization

Table 2. Air thermo-physical properties used in the simulations

Air Characteristics at Temperature (293.15 K)	
Density (kg/m³)	1.2047
Thermal conductivity (w/mk)	0.0255
Specific Heat (J/kgK)	1006.10
Viscosity (kg/ms)	1.8205e10-5
Thermal expansion (1/K)	0.00341
Boussinesq approximation Parameters	
Operative Temperature (K)	293.15
Operative Density at 293.15 K (kg/m³)	1.2047

Table 3. Thermo-physical properties of the material used in the simulations

Properties	Double-Glazed	Single-Glazed	Blinds
Density (kg/m3)	2500	2500	2719
Specific Thermal Capacity (J/kg- k)	840	840	871
Thermal Conductivity (W/m-k)	1.7	1.7	202.4
Absorption Coefficient (1/m)	(1285.7[a]) , (30[b])	(3000[a]) , (30[b])	-
Refraction Index (RI)	1.5	1.5	1.44
Emissivity	0.84	0.84	0.70

a) For wavelength 2.7-1000 nm
b) For wavelength 0.001-2.7 nm

Table 4. Considered mesh properties for mesh independency test

Mesh properties	Cell	Face	Nodes	Minimum Orthogonal Quality	Max Aspect Ratio	Average cavity air velocity-Boundary A	Average cavity air velocity-Boundary B
Coarse	22953	50756	24758	0.71	9.9	0.1156	0.1134
Medium	48886	105037	51674	0.71	6.4	0.1463	0.1310
Fine	99603	209446	103626	0.73	8	0.1571	0.1481
Finest	152276	319779	158367	0.74	8	0.1594	0.1499

Table 5. Absolute temperature differences between the models and measurements.

Sensors / Temperature (K)	#1	#2	#3	#4	#5	#6	#7	#8	#9	#10	Mean Bias Error (K)
$|T_A-T_{exp}|$	-	5.9	4.9	5.4	6.3	-	5.6	6.8	4.2	-	-4.9
$|T_B-T_{exp}|$	2.9	7.3	6	6.3	6.7	0.01	6	7.2	5.4	3.2	-5.2

Table 6. Absolute velocity differences between the models and measurements.

Sensors / Velocity (m/s)	#1	#2	#3	#4	#5	#6	#7	Mean Bias Error (K)
$|V_A-V_{exp}|$	0.226	0.078	0.138	0.175	0.045	0.011	0.006	-0.099
$|V_B-V_{exp}|$	0.204	0.053	0.103	0.175	0.041	0.053	0.060	-0.098

Table 7. Comparison between calculated average parameters for Boundary A and B

| Boundary Types	Average air velocity at the inlet (m/s)	Average air velocity at the outlet (m/s)	Average cavity air velocity (m/s)	Average outlet temperature (K)	Average cavity air temperature (K)	Airflow Rate (Kg/s)	Volume flow rate (m³/h)	Air-Change per hour (ach)	Extracted heat via outlet (W)
Boundary A	0.32	0.43	0.15	301.27	298.3	0.092	273.6	134	476.7
Boundary B	0.25	0.35	0.14	300.17	297.5	0.075	234	115	328.3
Difference	0.07	0.08	0.01	1.1	0.8	0.017	39.6	19	148.4

25
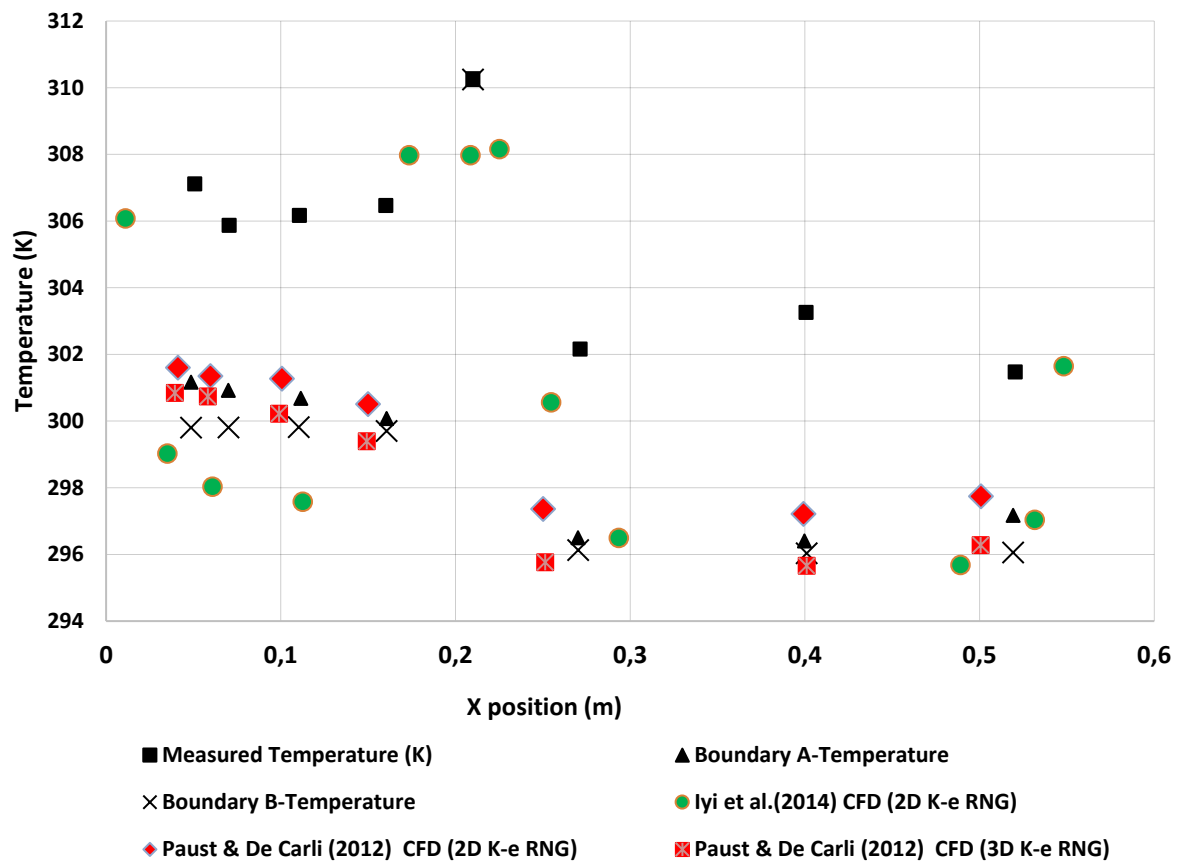
Figure 14.The comparison of temperature at the middle height of the cavity with the literature CFD simulations